Research Article | Vol. 8, No. 10 | 1 Oct 2017 | BIOMEDICAL OPTICS EXPRESS 4756
Biomedical Optics EXPRESS

Analysis of poration-induced changes in cells from laser-activated plasmonic substrates

NABIHA SAKLAYEN,[1,9,*] STEFAN KALIES,[2,3,4,9] MARINNA MADRID,[1] VALERIA NUZZO,[5] MARINUS HUBER,[6] WEILU SHEN,[1] JASMINE SINANAN-SINGH,[1,7] DAG HEINEMANN,[2,8] ALEXANDER HEISTERKAMP,[2,3,4,10] AND ERIC MAZUR[1,7,10]

[1]*John A. Paulson School of Engineering and Applied Sciences, Harvard University, Cambridge, MA 02138, USA*
[2]*Lower Saxony Centre for Biomedical Engineering, Implant Research and Development, Stadtfelddamm 34, 30625 Hannover, Germany*
[3]*Institut für Quantenoptik, Gottfried Wilhelm Leibniz Universität Hannover, Welfengarten 1, 30167 Hannover, Germany*
[4]*Cluster of Excellence REBIRTH, Hannover, Germany*
[5]*ECE Paris Ecole d'Ingénieurs, 75015 Paris, France*
[6]*Department of Physics, Ludwig Maximilian University of Munich, 80539 Munich, Germany*
[7]*Department of Physics, Harvard University, Cambridge, MA 02138, USA*
[8]*Industrial and Biomedical Optics Department, Laser Zentrum Hannover e.V., Hollerithallee 8, 30419 Hannover, Germany*
[9]*Co-first authors*
[10]*Co-last authors*
[*]*nsaklayen@gmail.com*

Abstract: Laser-exposed plasmonic substrates permeabilize the plasma membrane of cells when in close contact to deliver cell-impermeable cargo. While studies have determined the cargo delivery efficiency and viability of laser-exposed plasmonic substrates, morphological changes in a cell have not been quantified. We porated myoblast C2C12 cells on a plasmonic pyramid array using a 532-nm laser with 850-ps pulse length and time-lapse fluorescence imaging to quantify cellular changes. We obtain a poration efficiency of 80%, viability of 90%, and a pore radius of 20 nm. We quantified area changes in the plasma membrane attached to the substrate (10% decrease), nucleus (5 – 10% decrease), and cytoplasm (5 – 10% decrease) over 1 h after laser treatment. Cytoskeleton fibers show a change of 50% in the alignment, or coherency, of fibers, which stabilizes after 10 mins. We investigate structural and morphological changes due to the poration process to enable the safe development of this technique for therapeutic applications.

OCIS codes: (000.1430) Biology and medicine; (190.4870) Photothermal effects; (350.4855) Optical tweezers or optical manipulation.

References and links

1. C. E. Thomas, A. Ehrhardt, and M. A. Kay, "Progress and problems with the use of viral vectors for gene therapy," Nat. Rev. Genet. **4**(5), 346–358 (2003).
2. J. M. Meacham, K. Durvasula, F. L. Degertekin, and A. G. Fedorov, "Physical methods for intracellular delivery: practical aspects from laboratory use to industrial-scale processing," J. Lab. Autom. **19**(1), 1–18 (2014).
3. P. Mancheño-Corvo and P. Martín-Duque, "Viral gene therapy," Clin. Transl. Oncol. **8**(12), 858–867 (2006).
4. K. K. Ewert, A. Ahmad, H. M. Evans, and C. R. Safinya, "Cationic lipid-DNA complexes for non-viral gene therapy: Relating supramolecular structures to cellular pathways," Expert Opin. Biol. Ther. **5**(1), 33–53 (2005).
5. P. J. Canatella, J. F. Karr, J. A. Petros, and M. R. Prausnitz, "Quantitative study of electroporation-mediated molecular uptake and cell viability," Biophys. J. **80**(2), 755–764 (2001).
6. B. R. Davis, J. Yannariello-Brown, N. L. Prokopishyn, Z. Luo, M. R. Smith, J. Wang, N. D. Carsrud, and D. B. Brown, "Glass needle-mediated microinjection of macromolecules and transgenes into primary human blood stem/progenitor cells," Blood **95**(2), 437–444 (2000).
7. A. K. Shalek, J. T. Robinson, E. S. Karp, J. S. Lee, D.-R. Ahn, M.-H. Yoon, A. Sutton, M. Jorgolli, R. S.

#303310 https://doi.org/10.1364/BOE.8.004756
Journal © 2017 Received 25 Jul 2017; revised 23 Sep 2017; accepted 25 Sep 2017; published 27 Sep 2017

Biomedical Optics EXPRESS

Gertner, T. S. Gujral, G. MacBeath, E. G. Yang, and H. Park, "Vertical silicon nanowires as a universal platform for delivering biomolecules into living cells," Proc. Natl. Acad. Sci. U.S.A. **107**(5), 1870–1875 (2010).
8. G. C. Messina, M. Dipalo, R. La Rocca, P. Zilio, V. Caprettini, R. Proietti Zaccaria, A. Toma, F. Tantussi, L. Berdondini, and F. De Angelis, "Spatially, Temporally, and Quantitatively Controlled Delivery of Broad Range of Molecules into Selected Cells through Plasmonic Nanotubes," Adv. Mater. **27**, 7145 (2015).
9. S. Park, S. O. Choi, S. J. Paik, S. Choi, M. Allen, and M. Prausnitz, "Intracellular delivery of molecules using microfabricated nanoneedle arrays," Biomed. Microdevices **18**(1), 10 (2016).
10. D. Matsumoto, R. Rao Sathuluri, Y. Kato, Y. R. Silberberg, R. Kawamura, F. Iwata, T. Kobayashi, and C. Nakamura, "Oscillating high-aspect-ratio monolithic silicon nanoneedle array enables efficient delivery of functional bio-macromolecules into living cells," Sci. Rep. **5**(1), 15325 (2015).
11. A. Sharei, J. Zoldan, A. Adamo, W. Y. Sim, N. Cho, E. Jackson, S. Mao, S. Schneider, M.-J. Han, A. Lytton-Jean, P. A. Basto, S. Jhunjhunwala, J. Lee, D. A. Heller, J. W. Kang, G. C. Hartoularos, K.-S. Kim, D. G. Anderson, R. Langer, and K. F. Jensen, "A vector-free microfluidic platform for intracellular delivery," Proc. Natl. Acad. Sci. U.S.A. **110**(6), 2082–2087 (2013).
12. S. Feng, Z. Li, G. Chen, D. Lin, S. Huang, Z. Huang, Y. Li, J. Lin, R. Chen, and H. Zeng, "Ultrasound-mediated method for rapid delivery of nano-particles into cells for intracellular surface-enhanced Raman spectroscopy and cancer cell screening," Nanotechnology **26**(6), 065101 (2015).
13. G. Baffou, R. Quidant, and C. Girard, "Heat generation in plasmonic nanostructures: Influence of morphology," Appl. Phys. Lett. **94**(15), 153109 (2009).
14. O. Ekici, R. K. Harrison, N. J. Durr, D. S. Eversole, M. Lee, and A. Ben-Yakar, "Thermal analysis of gold nanorods heated with femtosecond laser pulses," J. Phys. D Appl. Phys. **41**(18), 185501 (2008).
15. D. Heinemann, M. Schomaker, S. Kalies, M. Schieck, R. Carlson, H. Murua Escobar, T. Ripken, H. Meyer, and A. Heisterkamp, "Gold nanoparticle mediated laser transfection for efficient siRNA mediated gene knock down," PLoS One **8**(3), e58604 (2013).
16. E. Y. Lukianova-Hleb, Y.-S. Kim, I. Belatsarkouski, A. M. Gillenwater, B. E. O'Neill, and D. O. Lapotko, "Intraoperative diagnostics and elimination of residual microtumours with plasmonic nanobubbles," Nat. Nano. **11**, 25–28 (2016).
17. R. Xiong, K. Raemdonck, K. Peynshaert, I. Lentacker, I. De Cock, J. Demeester, S. C. De Smedt, A. G. Skirtach, and K. Braeckmans, "Comparison of gold nanoparticle mediated photoporation: vapor nanobubbles outperform direct heating for delivering macromolecules in live cells," ACS Nano **8**(6), 6288–6296 (2014).
18. Y.-C. Wu, T.-H. Wu, D. L. Clemens, B.-Y. Lee, X. Wen, M. A. Horwitz, M. A. Teitell, and P.-Y. Chiou, "Massively parallel delivery of large cargo into mammalian cells with light pulses," Nat. Methods **12**(5), 439–444 (2015).
19. Z. Lyu, F. Zhou, Q. Liu, H. Xue, Q. Yu, and H. Chen, "Photoporation: A Universal Platform for Macromolecular Deliveryinto Cells Using Gold Nanoparticle Layers via the Photoporation Effect (Adv. Funct. Mater. 32/2016)," Adv. Funct. Mater. **26**(32), 5770 (2016).
20. E. Y. Lukianova-Hleb, E. Y. Hanna, J. H. Hafner, and D. O. Lapotko, "Tunable plasmonic nanobubbles for cell theranostics," Nanotechnology **21**(8), 085102 (2010).
21. S. Kalies, T. Birr, D. Heinemann, M. Schomaker, T. Ripken, A. Heisterkamp, and H. Meyer, "Enhancement of extracellular molecule uptake in plasmonic laser perforation," J. Biophotonics **7**(7), 474–482 (2014).
22. E. Bergeron, C. Boutopoulos, R. Martel, A. Torres, C. Rodriguez, J. Niskanen, J.-J. Lebrun, F. M. Winnik, P. Sapieha, and M. Meunier, "Cell-specific optoporation with near-infrared ultrafast laser and functionalized gold nanoparticles," Nanoscale **42**, 17836–17847 (2015).
23. M. Terakawa, M. Ogura, S. Sato, H. Wakisaka, H. Ashida, M. Uenoyama, Y. Masaki, and M. Obara, "Gene transfer into mammalian cells by use of a nanosecond pulsed laser-induced stress wave," Opt. Lett. **29**(11), 1227–1229 (2004).
24. E. Y. Lukianova-Hleb, X. Ren, J. A. Zasadzinski, X. Wu, and D. O. Lapotko, "Plasmonic Nanobubbles Enhance Efficacy and Selectivity of Chemotherapy Against Drug-Resistant Cancer Cells," Adv. Mater. **24**(28), 3831–3837 (2012).
25. C. M. Pitsillides, E. K. Joe, X. Wei, R. R. Anderson, and C. P. Lin, "Selective cell targeting with light-absorbing microparticles and nanoparticles," Biophys. J. **84**(6), 4023–4032 (2003).
26. C. Yao, R. Rahmanzadeh, E. Endl, Z. Zhang, J. Gerdes, and G. Huttmann, "Elevation of plasma membrane permeability by laser irradiation of selectively bound nanoparticles," J. Biomed. Opt. **10**(6), 064012 (2005).
27. S. Hashimoto, D. Werner, and T. Uwada, "Studies on the interaction of pulsed lasers with plasmonic gold nanoparticles toward light manipulation, heat management, and nanofabrication," J. Photochem. Photobiol. C Photochem. Rev. **13**, 28–54 (2012).
28. E. Boulais, R. Lachaine, and M. Meunier, "Plasma mediated off-resonance plasmonic enhanced ultrafast laser-induced nanocavitation," Nano Lett. **12**(9), 4763–4769 (2012).
29. D. Lapotko, "Optical excitation and detection of vapor bubbles around plasmonic nanoparticles," Opt. Express **17**(4), 2538–2556 (2009).
30. S. Kalies, D. Heinemann, M. Schomaker, H. Murua Escobar, A. Heisterkamp, T. Ripken, and H. Meyer, "Plasmonic laser treatment for Morpholino oligomer delivery in antisense applications," J. Biophotonics **7**(10), 825–833 (2014).
31. T. Mironava, M. Hadjiargyrou, M. Simon, V. Jurukovski, and M. H. Rafailovich, "Gold nanoparticles cellular toxicity and recovery: effect of size, concentration and exposure time," Nanotoxicology **4**(1), 120–137 (2010).

Biomedical Optics EXPRESS

32. I. Fratoddi, I. Venditti, C. Cametti, and M. V. Russo, "How toxic are gold nanoparticles? The state-of-the-art," Nano Res. **8**(6), 1771–1799 (2015).
33. S. Courvoisier, N. Saklayen, M. Huber, J. Chen, E. D. Diebold, L. Bonacina, J. P. Wolf, and E. Mazur, "Plasmonic Tipless Pyramid Arrays for Cell Poration," Nano Lett. **15**(7), 4461–4466 (2015).
34. N. Saklayen, M. Huber, M. Madrid, V. Nuzzo, D. I. Vulis, W. Shen, J. Nelson, A. A. McClelland, A. Heisterkamp, and E. Mazur, "Intracellular Delivery Using Nanosecond-Laser Excitation of Large-Area Plasmonic Substrate," ACS Nano **11**, 3671 (2017).
35. S. Kalies, G. C. Antonopoulos, M. S. Rakoski, D. Heinemann, M. Schomaker, T. Ripken, and H. Meyer, "Investigation of biophysical mechanisms in gold nanoparticle mediated laser manipulation of cells using a multimodal holographic and fluorescence imaging setup," PLoS One **10**(4), e0124052 (2015).
36. S. Kalies, S. Keil, S. Sender, S. C. Hammer, G. C. Antonopoulos, M. Schomaker, T. Ripken, H. Murua Escobar, H. Meyer, and D. Heinemann, "Characterization of the cellular response triggered by gold nanoparticle-mediated laser manipulation," J. Biomed. Opt. **20**(11), 115005 (2015).
37. A. A. Davis, M. J. Farrar, N. Nishimura, M. M. Jin, and C. B. Schaffer, "Optoporation and Genetic Manipulation of Cells Using Femtosecond Laser Pulses," Biophys. J. **105**(4), 862–871 (2013).
38. Z. Fan, H. Liu, M. Mayer, and C. X. Deng, "Spatiotemporally controlled single cell sonoporation," Proc. Natl. Acad. Sci. U.S.A. **109**(41), 16486–16491 (2012).
39. K. H. Jones and J. A. Senft, "An improved method to determine cell viability by simultaneous staining with fluorescein diacetate-propidium iodide," J. Histochem. Cytochem. **33**(1), 77–79 (1985).
40. Z. Qin and J. C. Bischof, "Thermophysical and biological responses of gold nanoparticle laser heating," Chem. Soc. Rev. **41**(3), 1191–1217 (2012).
41. R. Hobbie and B. Roth, *Intermediate Physics for Medicine and Biology* (Springer, 2015).
42. V. Zarnitsyn, C. A. Rostad, and M. R. Prausnitz, "Modeling Transmembrane Transport through Cell Membrane Wounds Created by Acoustic Cavitation," Biophys. J. **95**(9), 4124–4138 (2008).
43. P. L. McNeil and M. Terasaki, "Coping with the inevitable: how cells repair a torn surface membrane," Nat. Cell Biol. **3**(5), E124–E129 (2001).
44. C. A. Schneider, W. S. Rasband, and K. W. Eliceiri, "NIH Image to ImageJ: 25 years of image analysis," Nat. Methods **9**(7), 671–675 (2012).
45. J. M. Cooper, *The Cell* (ASM Press, 2009).
46. Z. Püspöki, M. Storath, D. Sage, and M. Unser, "Transforms and Operators for Directional Bioimage Analysis: A Survey," in *Focus on Bio-Image Informatics*, W. H. De Vos, S. Munck, and J.-P. Timmermans, eds. (Springer International Publishing, 2016), pp. 69–93.
47. R. Rezakhaniha, A. Agianniotis, J. T. C. T. C. Schrauwen, A. Griffa, D. Sage, C. V. C. V. C. Bouten, F. N. N. van de Vosse, M. Unser, and N. Stergiopulos, "Experimental Investigation of Collagen Waviness and Orientation in the Arterial Adventitia Using Confocal Laser Scanning Microscopy," Biomech. Model. Mechanobiol. **11**(3-4), 461–473 (2012).
48. E. Fonck, G. G. Feigl, J. Fasel, D. Sage, M. Unser, D. A. Rüfenacht, and N. Stergiopulos, "Effect of Aging on Elastin Functionality in Human Cerebral Arteries," Stroke **40**(7), 2552–2556 (2009).

Introduction

Effective membrane permeabilization of sensitive cell lines for cargo delivery is important for the advancement of fundamental biology research and new therapeutic applications. Among biological methods, viral transduction offers high efficiency but has limited cargo-carrying capacity and immunotoxicity risks [1–3]. Chemical methods such as lipofection have high throughput but vary in efficiency [4]. Electroporation, a physical method, offers high throughput and efficiency, but molecule uptake and cell viability are dependent on the field strength, pulse length, and pulse number in a complex manner [5]. Other physical methods such as microinjection and microfluidic squeezing offer a variety of advantages, but have low throughput and lack spatial selectivity, respectively [2,6–11]. Ultrasound-mediated methods transiently disrupt cell membranes to rapidly deliver molecules of interest, such as nanoparticles, drug molecules, and DNA fragments into the cytoplasm in a cost-effective manner [12]. However, the cavitation dynamics and membrane-associated pores are not spatially localized.

Several studies have analyzed laser-activated plasmonic nanostructures for the delivery of cell-impermeable cargo into cells [8,13–19]. Laser-activated plasmonic gold nanoparticles, which efficiently absorb laser light to form hotspots, cause heat-mediated bubbles in the liquid medium, which in turn form transient pores in cells for intracellular delivery [17,20–27]. Gold nanoparticles potentially outperform other physical techniques by offering high efficiency, viability, and throughput [21,28,29]. However, nanoparticles are sometimes ingested into the cell, which can have unwanted side effects at high concentrations [17,20,30–

Biomedical Optics EXPRESS

32]. Plasmonic substrate-based methods operate with the same physical poration mechanism as plasmonic nanoparticles but use lithography techniques to precisely pattern a surface of nanostructures that are not ingested by the cell. Recent studies have also shown that plasmonic substrates can deliver a broad range of cargo, including fluorescent probes, plasmids, bacteria, and proteins into cells [8,18,19,33,34]. Despite providing promising intracellular delivery results, the cellular changes induced by plasmonic substrates at the single cell level are not well understood [8,18,34]. To better understand and optimize the delivery process, it is important to analyze the induced membrane pores and associated cellular changes. Developing a biophysical understanding of the poration process by quantifying morphological cellular changes and studying how organelles behave after poration enables us to verify the safety of this technique for future applications [35,36].

In this study, we report measurements of cellular response to membrane permeabilization using pyramidal plasmonic substrates. We probe an adherent cell type (C2C12 myoblasts) that can be differentiated to investigate a second cell type (C2C12 myotubes). We use laser-activated plasmonic substrates consisting of template-stripped gold pyramids to induce membrane pores and study resulting changes in the area, cell position, pore size, morphology, and cytoskeleton behavior. We determine the experimental damage threshold of the substrate and the associated pyramid temperature. We quantify the permeabilization efficiency and viability of cells for various laser parameters and determine the pore radius to be 20 nm. We also investigate the cellular displacement over time and analyze the orientation of cytoskeletal fibers. Lastly, we confirm that plasmonic substrates porate cells in a spatially localized manner due to the delivery of cargo at specific sites in myotubes. In summary, our results contribute to a quantitative understanding of pore creation and cellular structural response to laser-exposed pyramidal plasmonic substrates.

2. Materials and methods

Pyramid fabrication and simulation model

Pyramids were fabricated by depositing 50-nm thin films of gold onto reusable silicon templates of inverted pyramids and template-stripping. Simulations were done using a temperature model in COMSOL. The geometry consists of a polymer pyramid on a glass substrate with a 50-nm gold film on top. Please see [34] for detailed fabrication steps and simulation model.

Cell culture labeling with dyes

C2C12 cells were cultured in Dulbecco's modified Eagle's Medium with high glucose containing 10% fetal calf serum and 1% penicillin streptomycin and incubated at 37 °C and 5% CO_2. Cells were passaged every other day and used for experiments at 50% confluence, between passage numbers 15 and 30. Cells were seeded on the substrate the day before experiments and placed in pre-warmed Phosphate Buffered Saline (PBS) for experiments for improved imaging.

For differentiation, cells were grown to confluency before the medium was changed to differentiation medium containing 1% horse serum, 1 μM insulin, and 1% penicillin streptomycin. Cells were differentiated for 5 days before experiments, and cell medium was exchanged every day during differentiation.

Calcein AM and propidium iodide were used for poration efficiency and viability experiments, as well as time-lapse imaging of in- and outflow of dyes to investigate pore dynamics. Both dyes have previously been used in literature to investigate flow in- and outside of cells [37,38]. We labeled C2C12 cells with 1 μM Calcein AM in PBS for 10 min at 37° C and washed once to reduce background fluorescence. Calcein AM is non-fluorescent initially due to an ester-bond-attached group (AM) that quenches fluorescence and makes the dye permeable to the plasma membrane. Once inside a viable cell, the quenching group is

Biomedical Optics EXPRESS

cleaved by intracellular esterases, leaving a membrane-impermeable, fluorescent dye molecule, Calcein, inside the cell. Propidium iodide was used at a concentration of 10 µM for inflow experiments as it can enter through the induced pores upon poration. This high concentration for inflow experiments was chosen to obtain a robust fluorescence signal at early time-points after cell perforation.

Membrane area changes were measured by staining cells with 40 µg/ml of WGA Alexa Fluor 488 for 10 min in the incubator before washing in PBS. The endoplasmic reticulum was pre-stained for 10 min with ER-tracker Red at a concentration of 1 µM, and left in the medium during the laser experiment.

For genetic labeling of Alpha-Actinin with red fluorescent protein, cells were transfected before the experiment with the plasmid tdTurboRFP-Alpha-Actinin-19 (Addgene plasmid # 58050, was a gift from Michael Davidson). The commercial reagent Viafect (Promega, US) was used for transfection with a DNA/Viafect ratio of 2:1, according to the manufacturer recommendations. Laser experiments were done the next day.

Laser and imaging setup

We imaged cells using a florescence microscope. The substrate was placed upside down on coverslip with 200 µL of PBS in between. The ensemble was placed on a motorized *x*-*y* translation stage (ProScan II, Prior Scientific, UK). A 40x 0.8-NA water-immersion microscope objective (Achroplan 40x/0.80 W, Carl Zeiss Microscopy GmbH, Germany) was placed upright under the coverslip. Fluorescence excitation was accomplished using a mercury vapor lamp (HBO 50, Carl Zeiss Microscopy GmbH). Calcein and WGA Alexa Fluor 488 imaging was done using a 480 ± 15 nm bandpass excitation filter and a 520 nm longpass emission filter. Propidium iodide and ER-tracker Red were excited using a (535 ± 20)-nm filter and detected with a (610 ± 25)-nm bandpass filter.

For laser exposure, a 532-nm pulsed Nd:YAG microchip laser with a pulse duration of 850 ps and repetition rate of 20.25 kHz was used. The laser spot diameter was 80 µm. The sample was exposed for fixed times using a mechanical shutter, and laser power was adjusted using an attenuation unit. A more detailed description of the setup can be found in [35].

Laser experiments and imaging with cells on substrates

Cell permeabilization efficiency is determined by varying the laser fluence for substrates in three independent experiments. Cells were seeded at 40% confluency on the substrates the day before experiments. On the day of the experiment, the substrate is pre-stained with Calcein AM. The substrate is placed gently upside down on 200 µL of PBS containing propidium iodide on a 66-mm coverslip (#1.5) without applying any external pressure. Surface tension holds the substrate and coverslip together. The substrate-coverslip construct is transferred to the imaging/laser exposure stage. The imaging setup is adjusted until cells pre-stained with Calcein AM could be seen in the focal plane to take a fluorescent image of cells before laser exposure. A mechanical shutter is used to irradiate a randomly selected area of cells with a fixed laser exposure time. Experiments were done at fluences of 8, 15, 21, 27, and 34 mJ/cm^2 combined with laser exposure times of 10, 20, and 40 ms. Two minutes after the experiment, the fluorescence channel was changed to image cells in the propidium iodide channel. The laser spot exposed on average 3 – 6 cells on the substrates. The cells were counted only if we observed that a visible part of their cytoplasm was clearly in the beam spot region. We counted the number of cells that had a propidium iodide signal in the beam spot, indicating the number of porated cells. We also counted the total number of cells that were present in the beam spot before laser exposure using calcein AM to pre-stain the cells. The efficiency was calculated by dividing the number of porated cells (Propidium Iodide) after laser exposure by the total number of cells before laser exposure (calcein AM channel).

Cell viability was determined by a separate set of experiments for varying fluences for three independent substrates. We first micromachined equidistant damage marks on the

Biomedical Optics EXPRESS

substrate at 70 mJ/cm^2 to locate where experiments were undertaken on the substrate. Before irradiation, cells were pre-stained with calcein AM, and laser exposure experiments were done just like above, without the addition of propidium iodide, as propidium iodide can be toxic [39]. Detailed images of the cells and substrates were recorded, in both fluorescent and brightfield imaging, and laser exposure was done in a spatially selective region to ensure that laser-exposed cells could be recognized later. Cells were incubated in cell media for 4 hours before being restained with calcein AM. The exact laser-exposed regions were found again for fluorescent imaging. Cells that did not show a calcein signal were either dead or detached from the surface of the substrate. We also counted the total number of cells that were present in the beam spot before laser exposure using calcein AM to pre-stain the cells. The viability was determined by dividing the number of cells that were present in the beam spot after laser exposure by the number of cells that were in the beam spot beforehand.

For differentiated cells, only poration data from cells that were directly in contact with the substrate were used for Fig. 6. This also makes the delivery efficiency extremely high, as targeting the right cell always results in poration.

For pore dynamics, experiments required pre-staining cells with Calcein AM (for outflow imaging) and adding propidium iodide (for inflow imaging) at the time of the experiment. Time-lapse imaging was started right before laser exposure of the cells. Images were taken at 10 fps for one min.

Experiments with WGA Alexa Fluor 488 and ER-tracker Red involved imaging several laser-exposed regions on the substrate at fixed intervals over one hour. The cells were cultured to be 80% confluent at the time of the experiment. We used a fixed laser fluence of 20 mJ/cm^2 and exposure of 10 ms for all experiments. We exposed 10 regions on the substrate in a row, with a center-to-center separation of 200 µm, using an *x*-*y* stage. An image of the cells was taken before laser exposure, and the timer was started at the time of laser exposure (timestamp: 0 min). An image was taken 30 s after laser exposure (timestamp: 0 min. 30 s) before moving to the next region. This was repeated for 10 regions. We then moved the stage to the site of the first laser-exposed region to take an image at the 10-min. timestamp, and repeated for all 10 regions. The imaging was then repeated for 30 min, and then again for 60 min. The experiment was repeated for 3 independent substrates. The fluorescence light was blocked between experiments to minimize photobleaching. One hour was the longest time we could have cells on the imaging setup before their viability began to reduce due to PBS evaporation through the open-air interface between the coverslip and substrate. In an initial series of experiments, we determined that 1h is the time period, which can be used without significant drying of the sample. Additionally, we used epi-fluorescence illumination for signal detection such that fluorescence from cells on the coverslip could be detected without any buffer in between. This ensured no influence of drying on the fluorescence signal.

For cytoskeleton experiments, cells that were expressing tdTurboRFP-Alpha-Actinin-19 were laser-exposed at a fluence of 20 mJ/cm^2 and laser exposure of 10 ms. Images were taken before laser exposure, and at 1 s, 60 s, 300 s, 600 s on the substrate. These experiments were limited to 600 cells to irradiate at least 5 cells per substrate and image them all. We repeated experiments on 5 cells on a substrate, three independent times.

Image analysis

For pore dynamics, we used ImageJ/FIJI to subtract the background from the stack of images. We traced the outline of the cell in a stack in ImageJ manually by eye and plotted the *z*-axis profile. The *z*-axis axis profile shows the fluorescence decay (Calcein) and growth (Propidium Iodide) that was used to calculate the pore size.

WGA Alexa Fluor images were analyzed to measure the change in the area of the membrane in the imaging plane. We did bleach correction (histogram matching), brightness adjustment, and template-matching on all images in the series. The cell outline was traced for

Biomedical Optics EXPRESS

each image at every time point, giving us the area of the membrane in the imaging plane. Three cells were analyzed in each laser-exposed region. Control experiments were repeated with cells on a flat glass coverslip in which all experimental steps were identical.

ER-tracker Red images were analyzed to measure the change in the fluorescent area of the endoplasmic reticulum, which is embedded in the cytoplasm and nucleus. We did bleach correction (histogram matching), brightness adjustment, and template-matching on all images in the series. The external ER-tracker Red region (which represents the cytoplasm) and the nuclear region was traced for each image at every time point and saved as a region of interest (ROI). We measured the area, position, short axis, and long axis for each cell. Three cells were analyzed in each laser-exposed region. Control experiments were done with cells on a flat glass coverslip in which all experimental steps were the same.

Alpha-Actinin images were analyzed to observe a potential change in orientation of cytoskeleton fibers in the cell. We did bleach correction (histogram matching), brightness adjustment, mean pixel processing for two pixels, and template-matching on all images in the series. An ROI (region of interest) was drawn around the cell. The OrientationJ measure function was used to measure the orientation and coherency inside the ROI.

In Figs. 2–5, the initial cell parameter value (no change) was measured and all acquired time series images were compared to this value.

Statistics

Statistical significance was determined using a two-sided Student's t-test. For box plots in Figs. 3, 4, and 5, the boxes represent the 25% and 75% quantile and whiskers represent the 5% and 95% quantile. The median is the straight line going across the box, and the mean is the small box within the larger box. The crosses represent the minimum and maximum for each data set. All data points show the mean and standard error of 5 cells in three independent samples.

3. Results and discussion

Imaging membrane permeabilization

We use an inverted fluorescence microscope to image C2C12 myoblast cells cultured on a plasmonic pyramidal substrate (Fig. 1(A)). An 850-ps laser source illuminates the substrate at a repetition rate of 20.25 kHz to generate plasmonic hotspots at the tip of each pyramid, leading to the formation of heat-mediated bubbles. The plasma membrane is transiently permeabilized, enabling the exchange of intra- and extracellular molecules.

We illuminated the substrate at different fluences and exposure times to determine the optical damage threshold. Laser exposure creates intense heating at the apex of each plasmonic pyramid. Brightfield imaging of the pyramidal substrate shows that damage begins to appear at a fluence of 27 mJ/cm^2 and a laser exposure time of 20 ms and 34 mJ/cm^2 with 10 ms exposure (Fig. 1(B) rows 1 – 3). We see larger damage regions with prolonged times due to the cumulative damage effect of many pulses. It is important to note that at a repetition rate of 20.25 kHz, heat is able to dissipate between each pulse, so no cumulative effects occur below the damage threshold. Single pulse temperature simulations show that the gold surface is heated up to the melting point of gold, which is 1063° C, Between a fluence 27 mJ/cm^2 and 34 mJ/cm^2 (Fig. 1(B) row 4) [40].

To determine the plasma membrane permeabilization efficiency and cell viability, we pre-stained cells with calcein AM and added propidium iodide at the time of laser exposure (Fig. 1(C)). Propidium iodide is a cell-impermeable dye that binds to nucleic acid upon entering the cell. A decrease in calcein AM signal after laser exposure indicates intracellular molecules flowing out of the cell, and an increase in propidium iodide signal indicates extracellular molecules flowing into the cell. We account for photobleaching during image processing by normalizing the brightness. We did not observe significant photobleaching in the first 2

Biomedical Optics EXPRESS

frames after a laser exposure of milliseconds, and calcein AM outflow occurred over tens of seconds. Calcein AM pre-staining enables us to determine exactly how many cells are exposed in the laser spot, permitting us to determine efficiency. The propidium iodide signal due to an influx of molecules into the cell also confirms that the plasma membrane is permeabilized. The efficiency peaks at 80% at a fluence of 27 mJ/cm^2 and exposure of 20 ms, matching the damage threshold of the pyramidal substrate without cells (Fig. 1(D)). Laser-irradiated cells are tested for viability 4 h later using calcein AM and propidium iodide. The viability remains around 90% for fluences below 27 mJ/cm^2, starts to drop, and is lowest at a high fluence at or above 34 mJ/cm^2 (Fig. 1(E)). Effective permeabilization using substrates requires fluences ranging 20 – 40 mJ/cm^2 for delivery efficiencies of 80%, which is comparable to gold nanoparticles at equal laser parameters [15,36].

According to simulations, the onset of poration agrees well with the spinodal threshold of bubble formation at 305 °C, which is approximately 90% of the critical point in water [40]. Simulations indicate that the bubble-forming threshold is reached between 8 mJ/cm^2 and 15 mJ/cm^2. 21 mJ/cm^2 is the threshold fluence used for the remainder of cell experiments in this paper to remain both above the bubble formation threshold (8 mJ/cm^2), and below the experimental damage threshold (27 mJ/cm^2) (Fig. 1(B)).

Biomedical Optics EXPRESS

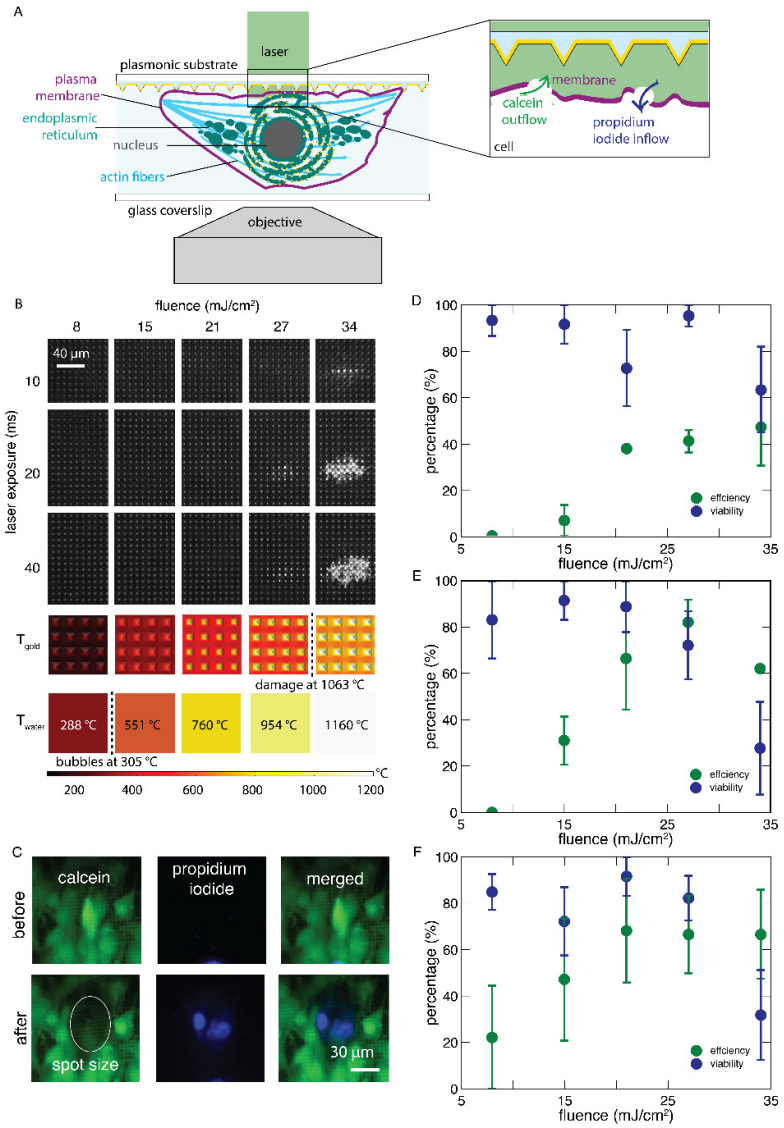

Fig. 1. Using plasmonic substrates to investigate plasma membrane poration of differentiating myoblasts with fluorescent imaging. ***(A)*** The experimental setup consists of an 850-ps laser source illuminating a plasmonic pyramidal substrate consisting of uniform base lengths (2.4 µm), heights (1.4 µm), and base to base spacings (1.2 µm) with adherent C2C12 cells. The substrate-cell composite is placed upside down on a glass coverslip with 200 µL of phosphate-buffered saline containing propidium iodide. The assembly is placed on an objective for fluorescence imaging. The inset shows laser-induced poration, enabling the exchange of intra- and extracellular molecules. ***(B)*** Shows bright-field images of the pyramidal substrate exposed at different laser fluences and exposure times to determine the optical damage threshold of the plasmonic substrate. At the bottom are single laser shot simulation results of the temperature of the gold pyramids and surrounding water. ***(C)*** Cells pre-stained with Calcein AM confirm plasma membrane poration. A decrease in calcein signal after laser exposure indicates outflow of intracellular molecules, while an increase in propidium iodide signal indicates inflow of extracellular molecules. The poration efficiency of C2C12 as a function of fluence for different laser exposures: (***D***)10 ms, (***E***) 20 ms, and (***F***) 40 ms. Data show standard error of the mean for three independent measurements with around 3-6 cells in each spot.

Biomedical Optics EXPRESS

Pore size and kinetics

The number of molecules entering through pores in the plasma membrane is determined by the diffusivity of the molecule and by number and size of the induced pores and the time they remain open. The pore dynamics not only affect the delivery efficiency, but also affect membrane recovery. We measured calcein outflow and propidium iodide inflow to determine the size of the pores (Fig. 2(A)). Time-lapse imaging of C2C12 cells shows a decrease in fluorescence from calcein (molecular weight 623 Da) and an increase in fluorescence from propidium iodide (670 Da) (Fig. 2(B)). Figure 2(C) shows the time-dependence of the relative fluorescence of calcein and propidium iodide in a single cell. The cell shows a reduction from a relative fluorescence value of 1 to 0.4 for calcein over 30 s and an increase from 0.3 to 1 for propidium iodide over 60 s (Fig. 2(C)). These timescales are different because calcein is a small diffusive dye molecule, whereas it takes additional time for the propidium iodide to bind with a nucleic acid complex [38].

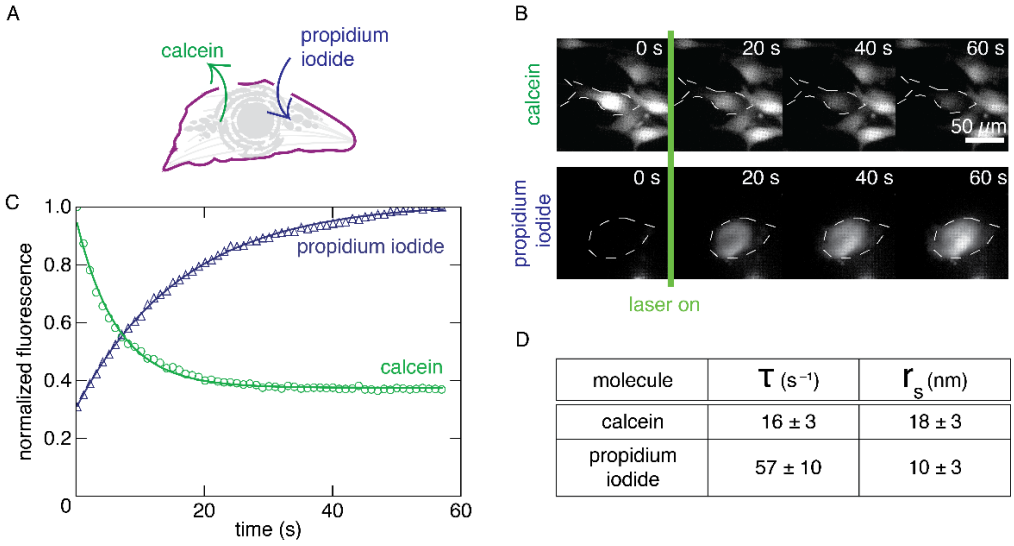

molecule	τ (s^{-1})	r_s (nm)
calcein	16 ± 3	18 ± 3
propidium iodide	57 ± 10	10 ± 3

Fig. 2. Determining the pore size using time-lapse imaging. ***(A)*** Calcein outflow and propidium iodide inflow. ***(B)*** Time-lapse imaging of C2C12 cells to determine the decrease in fluorescence over time at 10 frames per second (fps) for 60 s. Outlines of cells show the region in which fluorescence signal is measured. ***(C)*** Relative fluorescence of calcein and propidium iodide over time. The data is fitted to Eq. (2). ***(D)*** Data showing in/outflow exponential constants τ and a pore radius r_s of 18.4 ± 2.9 nm with calcein and 9.7 ± 3.4 nm with Propidium Iodide. Numbers obtained from three independent experiments, using five cells for each experiment.

To determine the pore radius from these data, we consider a substrate-induced hole of radius r in the plasma membrane [37]. As proposed by Davis *et al.* [37], we take the radius r to be constant during the time it is open before closing rapidly. The dye concentration in the cell $\Phi(t)$ then changes exponentially:

$$\Phi(t) = \Phi(0)\exp\left(-\frac{t}{\tau}\right), \tag{1}$$

where $\Phi(0)$ is the initial fluorescence, t is the time, an τ is the decay/growth constant. The flow through the hole is given by [41]:

Biomedical Optics EXPRESS

$$\frac{d\Phi(t)}{dt} = \frac{\pi r^2 D}{\left(Z + \frac{2\pi r}{4}\right)V}\Phi(t) \ , \tag{2}$$

where D is the diffusion coefficient, ΔZ is the membrane thickness, and V is the volume of the cell. Using a diffusion coefficient D of 3.64^{-10} m^2/s for calcein and a cell volume V of 1200 μm^3 [37], we obtain the hole radius r from the decay/growth constant in Eq. (2):

$$\tau = \frac{(Z + \frac{2\pi r}{4})V}{\pi r^2 D} \ . \tag{3}$$

Davis *et al*. consider a single pore forming in the cell, whereas the plasmonic substrates used in this work induce multiple pores. Given the large pyramids peak-to-peak spacing of 1.6 µm, we assume that each pyramid induces a separate pore, and we take the radius of an individual pore to be $r_s = r/\sqrt{N}$, where N is the number of pyramids within the laser-exposed cell area. This approach yields a pore size of 18 ± 3 nm using the calcein data and 10 ± 3 nm using the propidium iodide data. We assume that both molecules diffuse through similar pores. The difference in value can be attributed to the slower rate of diffusion of propidium iodide, which only fluoresces upon binding to nucleic acids within the cell — a fact not accounted for in the pore size model. The propidium iodide diffusion would be mediated by the molecule itself and by the bound nucleic acid, while calcein diffuses independently. However, both values are of the same order of magnitude.

The pore radius sizes are in agreement with experiments delivering dextran molecules that have a Stokes radius in the range of 20 nm [21,34]. Membrane resealing occurs at this pore size [42,43]. However, a large number of simultaneous larger pores on the membrane leads to cell death at high fluences. About 70–80 pyramids contribute to the poration for each cell. Since the pyramids have a peak-to-peak spacing of 1.6 µm, each pyramid leads to an individual pore. We assume that due to this large spacing, it is possible to treat all fluid below the cell and in between the pyramids as bulk fluid. However, as the pyramid tips are attached to the cell and might influence or hinder some inflow of molecules, our calculated pore size may be slightly underestimated.

Cell morphology changes

The in- and outflow of molecules through transient pores in the plasma membrane can change the cell's structure to a point where the cell is unable to maintain homoeostasis. We analyze morphology alterations in the plasma membrane and endoplasmic reticulum (ER) to quantify area changes in the membrane, cytoplasm, and nucleus.

We image the plasma membrane area, cytoplasmic area, and nuclear area before and after laser exposure. We measure these changes at specific time intervals of 30 s, 10 min, 30 min, and 60 min (Fig. 3(A)). The plasma membrane is fluorescently labeled with Wheat Germ Agglutinin (WGA) Alexa Fluor 488 to highlight the surface of the cell. We measure changes in the cytoplasm and nucleus with an endoplasmic reticulum dye, ER-tracker Red, as it shows both the nuclear envelope and the extent of the cytoplasm.

Image analysis shows that laser exposure causes a 10% decrease in plasma membrane area, which stabilizes after 30 min. No statistically significant change is seen after 60 min (p = 0.26, Fig. 3(B)). The cytoplasmic area decreases about 5–10% after laser exposure, and the decrease remains statistically significant until 60 min, the maximum duration observed experimentally (Fig. 3(C)). The cytoplasm area changes are related to pressure alterations as materials escape through pores and the cytosol has to structurally rearrange itself. The nuclear area also decreases 5–10% after laser exposure, but the change after 30 minutes is not statistically significant (p = 0.15, Fig. 3(D)). The drop in the nuclear area indicates pore

Biomedical Optics EXPRESS

formation in the nucleus or that the nuclear membrane was deformed. As indicated by the percentage of total cell area decrease and cytoplasmic/nuclear decrease, we observe no significant change in the ratio of nuclear to the cytoplasmic area after laser exposure ($p > 0.32$).

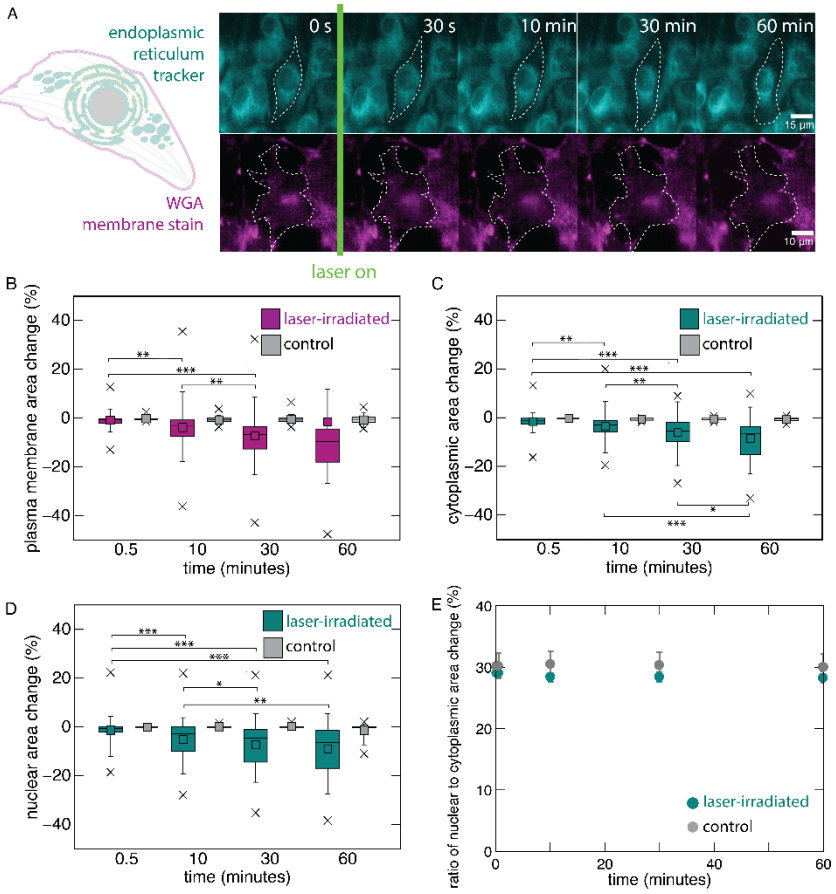

Fig. 3. Cell morphology: changes in plasma membrane area, cytoplasmic area, and nuclear area. ***(A)*** Schematic representation showing different regions of the cell that are fluorescently labeled. Cells were imaged at 30 s, 10 min, 30 min, and 60 min after laser exposure. (***B)*** The plasma membrane area attached to the pyramidal surface decreases due to laser exposure but stabilizes after 30 min. Boxes represent the 25% and 75% quantile and whiskers represent the 5% and 95% quantile. The straight line across the box represents median and small square box represents mean. Crosses represent minimum and maximum in each data set. ***(C)*** Laser-induced decrease in cytoplasmic area due to laser exposure (statistically significant until 60 min.). ***(D)*** Laser-induced decrease in nuclear area (not statistically significant after 30 min.). ***(E)*** Ratio of nuclear to cytoplasmic area (three independent experiments, with 10 cells each). * = $p < 0.05$; ** = $p < 0.01$; *** = $p < 0.001$.

We investigate if structural changes triggering cellular locomotion as displacement would further confirm internal cytosolic rearrangement. If the cells would only shrink in area, they would remain almost at the same position. To study repositioning of the cell, we defined three position properties: the center of mass position, long axis, and short axis (Fig. 4(A)). These were all determined by outlining the cell in ImageJ, and using customized macros to calculate these characteristics. The center of mass is a brightness-weighted average of the x and y coordinates of all pixels in the cell. The short and long axes are determined from an oval drawn around the cell [44].

Biomedical Optics EXPRESS

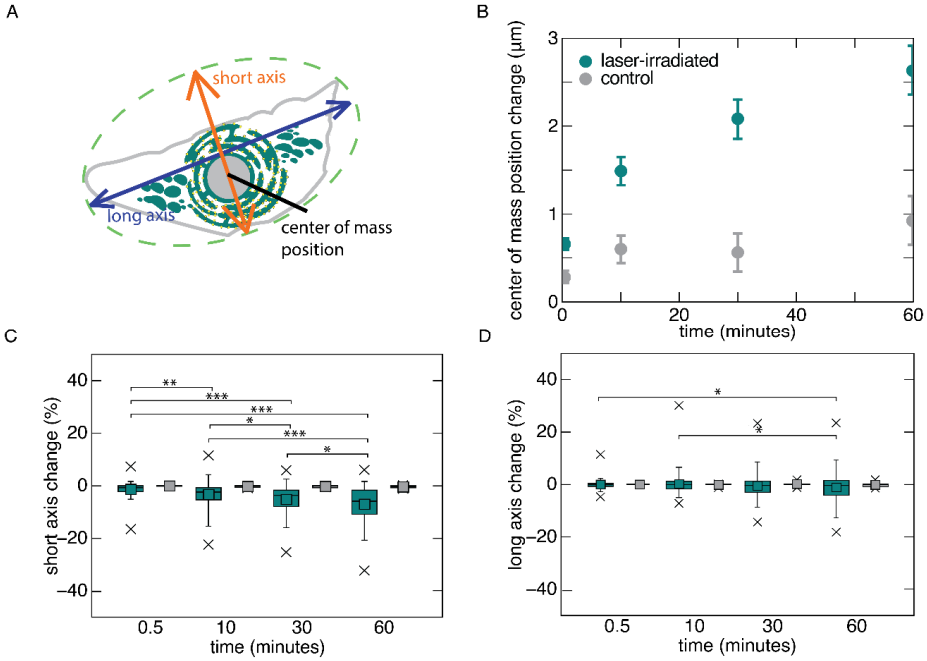

Fig. 4. Cellular displacement and repositioning. ***(A)*** Position properties measured: center of mass position, long axis, and short axis. ***(B)*** Time-dependence of relative center of mass. ***(C)*** Change in short-axis length over time. ***(D)*** Change in long-axis length over time. Boxes represent the 25% and 75% quantile and whiskers represent the 5% and 95% quantile. The straight line across the box represents median and small square box represents mean. Crosses represent minimum and maximum in each data set. Data obtained from three independent experiments, with 10 cells each. * = $p < 0.05$; ** = $p < 0.01$; *** = $p < 0.001$.

Figure 4(B) shows the change in center of mass position over 1 h after laser exposure. The data show that, unlike unexposed cells, laser-exposed cells move away from their original location by 2 – 3 μm after 1 hr. Unexposed cells moved around 1 μm over an hour. The displacement confirms that structural rearrangements did occur within the cytoplasm. The short axis changes by an average of 7% over 1 h, and the change is statistically significant ($p = 0.024$, Fig. 4(C)); the long axis shortens minimally after laser exposure; the long axis length at 30 min does not differ significantly from 60 min ($p = 0.22$, Fig. 4(D)). The short axis changes more than the long axis as the cells have more actin fibers along the long axis, making it harder for changes to occur in that direction.

Structure of the cytoskeleton

We investigated the dynamic response of the cytoskeleton fibers. The cytoskeleton consists of a network of actin filaments and associated actin-binding proteins that determines the cell's ability to move after experiencing membrane permeabilization [45]. Using cells expressing RFP-labeled alpha-actinin, we studied changes in orientation of fibers in the cytoskeleton before and during a 10-minute time interval after laser exposure. We determined the orientation of the fibers from fluorescent images (Fig. 5(A)) [46–48] and calculated the coherency in fiber orientation; a coherency of one indicates that the fibers are perfectly aligned in one direction, and a value of zero indicates random alignment [46]. As shown in Fig. 5(B) the coherency drops sharply immediately after laser exposure, but stabilizes over the course of 1 – 5 minutes, indicated by the absence of further changes (Fig. 5(B)). The structural changes are related to the membrane resealing phase of permeabilization [42,43]. Despite undergoing a quick change in the first seconds after laser exposure, the cytoskeletal structure recovers rapidly and remains intact over time, which is important for cell survival.

Biomedical Optics EXPRESS

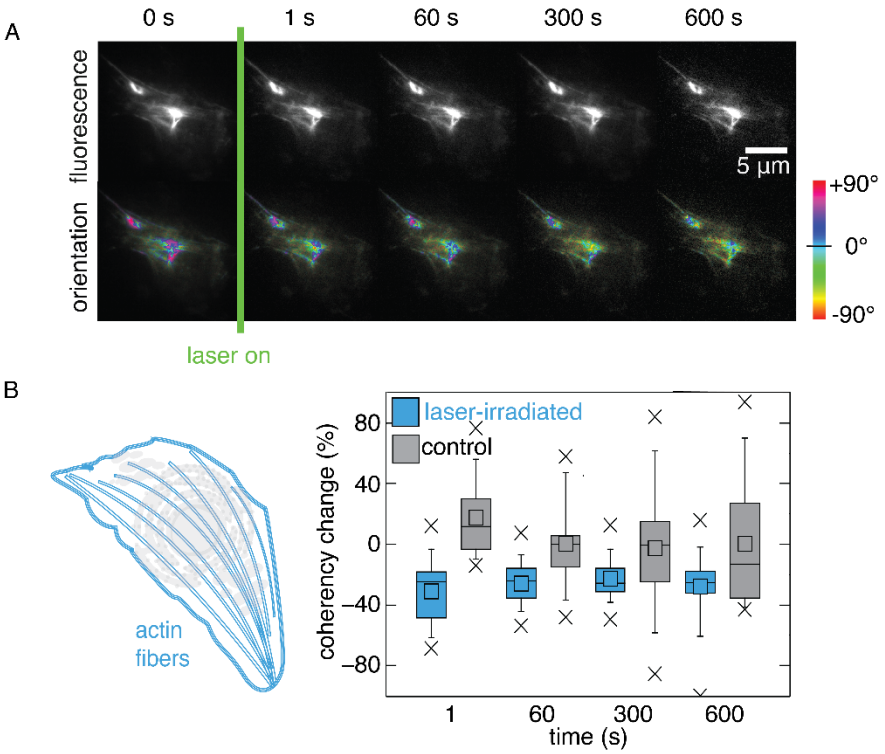

Fig. 5. Cytoskeleton orientation. ***(A)*** Fluorescent imaging of the cytoskeleton before and after laser exposure and calculated fiber orientation of fibers in the cytoskeleton. ***(B)*** Change in fiber orientation over time. Boxes represent the 25% and 75% quantile and whiskers represent the 5% and 95% quantile. The straight line across the box represents median and small square box represents mean. Crosses represent minimum and maximum in each data set. Data obtained from three independent experiments, with 10 cells each; *p*-values all greater than 0.05.

Influence of the substrate-cell distance and cell type on poration

To study the effect of the substrate-cell distance and cell type on poration, we differentiated C2C12 myoblast on the substrate to form C2C12 myotubes, which are elongated in morphology (Fig. 6(A)). As these differentiate and grow in layers, only specific segments of a myotube are in close contact with the plasmonic substrate. Consequently, we only observed permeabilization in these specific segments of the cell upon laser exposure (Figs. 6(A) and 6(B)). The inflow of propidium iodide was limited to these regions (shown in circled regions) and diffusion out of the laser irradiated region was strongly limited. The required fluence for efficient permeabilization was in the same range as for C2C12 myoblasts (Fig. 6(C)).

Biomedical Optics EXPRESS

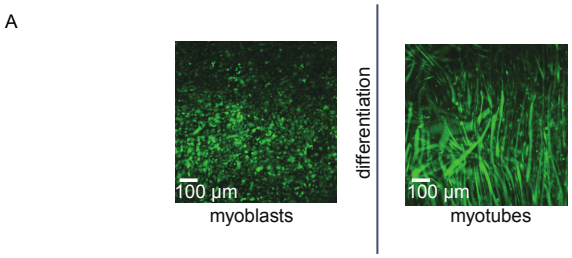

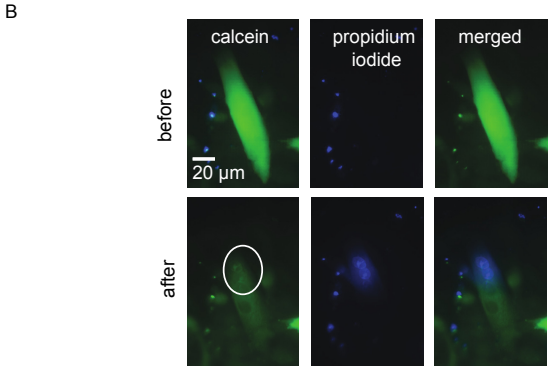

C

fluence (mJ/cm^2)	efficiency (%) 10 ms exposure	efficiency (%) 20 ms exposure	efficiency (%) 40 ms exposure
21	0	83 ± 17	50 ± 29
27	100	100	100
34	100	100	100

Fig. 6. Membrane permeabilization of differentiated myotubes. ***(A)*** Differentiation of C2C12 myoblasts on the substrate to make longer C2C12 myotube cells. ***(B)*** Poration due to laser exposure. Propidium iodide delivery is limited to the laser-exposed area. ***(C)*** Fluence-dependence of the membrane poration efficiency for different laser exposures. Data obtained from three independent experiments, with three cells each.

4. Conclusions

We develop a biophysical understanding of the poration process by quantifying changes in living cells. We used fluorescence microscopy to analyze laser-induced poration of C2C12 cells on plasmonic substrates. The efficiency of small molecule delivery peaks at 80% with a viability of 90%. The resulting pore radius is in the range of 10–20 nm, which would decrease by 5–10% after laser exposure, and stabilizes after 30 min. The plasma membrane area decreases by 5–10%, but stabilizes after 1 hr. The cytoplasmic area changes by 5–10% and continues to change after 1 hr. The center of mass positions shift by 2 – 3 µm after 1 hr. and the width of the cell shrinks by 7% due to poration-induced spatial rearrangements. Cytoskeleton fibers change their alignment by 50%, before stabilizing after 10 mins. Additionally, we delivered cargo into specific regions of differentiated C2C12 myotubes, confirming spatially localized poration. Developing a biophysical understanding of the poration process enables the safe development of this technique for therapeutic applications.

Biomedical Optics EXPRESS

Funding

NS, MM, WS, JSS, and EM were supported by the National Science Foundation under contracts PHY-1219334 and PHY-1205465. NS was funded by the Howard Hughes Medical Institute's International Fellowship and the short-term research fellowship from DAAD. MM was funded by the Graduate Prize Fellowship at Harvard University. SK and AH received funding from the German Research Foundation through the Cluster of Excellence REBIRTH (DFG EXC62/3). Parts of this work were carried out as an integral part of the BIOFABRICATION FOR NIFE Initiative, which is financially supported by the ministry of Lower Saxony and the Volkswagen Stiftung (BIOFABRICATION FOR NIFE: VWZN2860). NN, MM, and EM have an interest in Cellino Biotech.

Acknowledgments

NS, and SK, designed and carried out the experiments, and analyzed the results. MM and JSS fabricated the templates and substrates. MH simulated the laser-substrate interaction. AH and EM supervised the research and the development of the manuscript. NS wrote the first draft of the manuscript; all authors subsequently took part in the revision process and approved the final copy of the manuscript. NS and SK contributed equally to work.

Substrate fabrication was done at the Center for Nanoscale Systems at Harvard University. Laser Experiments were done at NIFE – Niedersächsisches Zentrum für Biomedizintechnik, Implantatforschung und Entwicklung in Germany.

Disclosures

NS, MM, EM: Cellino Biotech (P,S). The other authors declare that there are no conflicts of interest related to this article.